ATMOSPHERIC SCIENCE

Anthropogenic warming induced intensification of summer monsoon frontal precipitation over East Asia

Suyeon Moon[1,2], Nobuyuki Utsumi[3,4], Jee-Hoon Jeong[5], Jin-Ho Yoon[6], S.-Y. Simon Wang[7], Hideo Shiogama[8], Hyungjun Kim[1,2,9,10]*

Summer monsoon frontal rainfall in East Asia (EA) is crucial for water resources and flood hazards in densely populated areas. Recent studies have documented the increasing intensity of summer frontal rainfall over recent decades. However, the extent of ongoing climate change on the intensification of the EA frontal precipitation system remains uncertain. Using an objective method for detecting frontal systems, we found a 17 ± 3% increase in observed frontal rainfall intensity during 1958 to 2015. Climate model simulations with and without greenhouse gases suggest that anthropogenic warming plays a key role in the intensification of EA summer frontal precipitation by 5.8% from 1991 to 2015. The analysis highlights that enhanced water vapor convergence and reinforced western North Pacific subtropical High collectively increased moisture transport to the region, resulting in intensified EA frontal precipitation. The results lend support to the anthropogenic warming–induced enhancement of the EA frontal precipitation and its persistence in the future.

INTRODUCTION

East Asian (EA) summer precipitation brings much-needed water for agriculture, industry, and life. In recent decades, the intensity and frequency of heavy rainfall over EA have increased (*1*–*4*). Satellite observations indicated an increasing trend of the frequency of summer extreme precipitation along the Meiyu-Baiu front (*4*). For example, the unprecedented frontal heavy rainfall in July 2018 resulted in 221 fatalities in Japan and destroyed 6296 buildings (*5*). That event exhibited an increased moisture transport from the tropics and strong large-scale ascending motion over EA (*6*). The 2020 Meiyu season that caused catastrophic rainfall in the Yangtze River in China marked a new record since 1961 while displacing 63 million people and causing about 16 billion U.S. dollars of economic losses (*4*, *7*–*9*). In the summer of 2020, extremely long and heavy rainfall in South Korea led to 44 fatalities and about a billion U.S. dollars of economic losses (*1*, *10*). In August 2022, the record-breaking summer frontal rainfall caused a deadly flood in a densely populated and economically developed district in Seoul, South Korea, an event that was the highest in 115 years since weather observations started (*11*). Whether these episodes can be explained by natural variability or the influence of anthropogenic warming is unclear. We aim to provide a comprehensive explanation for the changes in the mechanisms and the roles of anthropogenic climate change (*1*, *12*, *13*) and natural variability (*8*, *14*) on the observed trend in the EA summer rainfall.

The EA summer rainfall is a result of various weather systems such as typhoons, extra-tropical cyclones, fronts, and others (*15*, *16*). Here, we focus on front-related rainfall, which accounts for about 40% of the EA summer rainfall (*17*). Summer monsoon front over EA (hereafter, EASM front), called the Changma-Meiyu-Baiu front, is an essential weather system producing heavy rains (*15*, *18*–*20*). The EASM front features a convergence of moisture along the western North Pacific subtropical High (WNPSH) and Okhotsk High (*20*–*22*). During the summer season, the stepwise northward movement of the front induces an onset of the EA summer monsoon along its path, periodically evoking heavy rain and flooding disasters (*2*, *23*). Since many mega-cities such as Seoul, Shanghai, and Tokyo are located on the migration pathway of the EASM front, understanding the changes in the precipitation events and underlying mechanisms is crucial for disaster prevention.

The impact of climate change on the EA water cycle intensity during summer has been studied extensively (*12*, *24*–*29*). On the basis of the observation and multimodel simulations such as the Coupled Model Intercomparison Project (CMIP), the heavy rainfall intensity (*12*, *24*–*26*) and frequency (*1*) over EA have shown an increase due to atmospheric warming and moistening. Nonetheless, a synoptic perspective has been missing, as most previous studies only focused on the seasonal or areal mean of the changes in rainfall patterns.

In this study, we identified monsoonal fronts and associated frontal rainfall with an objective detection method by combining observational and simulation datasets (see Materials and Methods; figs. S1 and S2). We explored how anthropogenic greenhouse gas forcing modified the frontal rainfall intensity (FRI) during the historical period of 1958–2015. The anthropogenic greenhouse gas forcing is known to have a robust impact on precipitation systems (*25*, *30*, *31*). To determine the anthropogenic greenhouse gas forcing impacts, we used the Community Earth System

[1]Moon Soul Graduate School of Future Strategy, Korea Advanced Institute of Science and Technology, Daejeon, South Korea. [2]Institute of Industrial Science, University of Tokyo, Tokyo, Japan. [3]School of Environment and Society, Tokyo Institute of Technology, Tokyo, Japan. [4]Nagamori Institute of Actuators, Kyoto University of Advanced Science, Kyoto, Japan. [5]Department of Oceanography, Chonnam National University, Gwangju, South Korea. [6]School of Earth Sciences and Environmental Engineering, Gwangju Institute of Science and Technology, Gwangju, South Korea. [7]Department of Plants, Soils and Climate, Utah State University, Logan, UT, USA. [8]Earth System Division, National Institute for Environmental Studies, Tsukuba, Japan. [9]Department of Civil and Environmental Engineering, Korea Advanced Institute of Science and Technology, Daejeon, South Korea. [10]Graduate School of Green Growth and Sustainability, Korea Advanced Institute of Science and Technology, Daejeon, South Korea.
*Corresponding author. Email: hyungjun.kim@kaist.ac.kr

Model version 1 Large Ensemble (CESM1-LE) (*32*) projections (see Materials and Methods) with historical (HIST) and all-but-greenhouse gas forcing (XGHG) experiment. It allows the attribution analysis of the changes in the frontal precipitation system with respect to the contributions of greenhouse gas emissions.

RESULTS

Observed changes in frontal rainfall intensity

The monsoonal front was defined by an objective detection algorithm based on the meridional gradient of equivalent potential temperature at 850 hPa (see Materials and Methods). Previously, frontal identification often relied on subjective detection algorithms (*33*) without systematic verification, which can lead to misclassification of the front and erroneously associated rainfall (*18*, *19*). In this study, we carefully validated the detected fronts against the digitized front map (*17*) derived from the Japanese Meteorological Agency surface weather chart (Supplementary Text and figs. S1 and S2). Using observational gridded precipitation data [Asian Precipitation–Highly Resolved Observational Data Integration Towards Evaluation of Water Resources (APHRODITE) Monsoon Asia (*34*), see Materials and Methods], precipitation with grid rainfall > 1 mm/day falling within a 500 km radius of the front from June 16 to July 15 is considered to be EASM frontal rainfall for the period of 1958–2015 (*4*, *17*, *35*).

The changes in total frontal rainfall over EA between the earlier (1958–1982) and the later (1991–2015) periods were assessed from the global reanalysis and observational rainfall datasets. On the basis of the observational dataset, we observed a substantial increase of 21.3% in total frontal rainfall between these periods (fig. S3A). To further explore the changes in total frontal rainfall, we decomposed them into frequency and intensity for each period (see Materials and Methods) (*15*). It was found that the increase in frontal rainfall was largely contributed by the intensity (92%) change (Fig. 1, A and B), while the contribution of frequency changes was marginal (6%) (Fig. 1B and fig. S3). Along the coastal regions of EA, from eastern China to southwestern Japan (box in Fig. 1A), observations showed that the intensity of frontal rainfall became substantially enhanced (+17 ± 3%). Specifically, when using the APHRODITE and Rainfall Estimates on a Gridded Network (REGEN) datasets, there was a +19.8% increase in FRI (fig. S4D) and a +14.2% increase (fig. S4C), respectively. Note that the occurrence of front and frontal rainfall shows relatively minor changes (figs. S5 and S6). These observed enhancements of FRI suggested a combined effect from natural variability and anthropogenic forcing (*36*). However, the observed data is not long enough to distinguish the anthropogenic forcing effect.

Detection of anthropogenic greenhouse gas forcing impact

We explored the spatial patterns of change in the frontal rainfall as a response to greenhouse gas forcing by using large-ensemble simulations. To reveal the anthropogenic greenhouse gas forcing effect, Fig. 1C shows the differences between the HIST and the XGHG experiments. The spatial pattern of the simulated changes in FRI is comparable to that of the observed changes between the earlier and later periods, with a pattern correlation coefficient (PCC) of 0.4 (Fig. 1A). It appears that the enhancement of FRI dominates the features of change in the total rainfall under the greenhouse gas forcing during the recent period (1991–2015) (fig. S7), and that greenhouse gas forcing intensified the mean frontal rainfall by 5.8% during the later period (Fig. 1C). When we consider land areas only, the intensity of frontal rainfall exhibited a 4.9% increase attributed to the impact of the anthropogenic greenhouse gas forcing effect (fig. S8). Furthermore, it is noteworthy that the HIST experiment exhibited higher warming pattern (+0.9 K) compared to the XGHG experiment, further highlighting the differences between the two simulations (fig. S9). There is relatively little change in the location of the monsoon front (fig. S2, B and C).

The extreme side of the frontal rainfall distribution is more sensitive to the greenhouse gas forcing than its average (*37*). To quantify the impact of anthropogenic greenhouse gas on the probability of frontal extreme rainfall events, we derived the risk ratio (RR) and the fraction of attributable risk (FAR) as the ratio of occurrence probability between the HIST (P_{HIST}) and XGHG (P_{XGHG}) experiments (see Materials and Methods). These were calculated for the 95th and 99th percentile thresholds of FRI under the XGHG experiment, respectively (Fig. 1D; defined as RR_{95} and RR_{99}). The chance of encountering a heavy frontal rainfall event at the 95th percentile was 2.84 times higher [RR_{95}; 5 to 95% confidence interval (CI) 2.58 to 2.95] compared to that of a world without greenhouse gas emissions. Furthermore, the risk of the extreme event at the 99th percentile increased by 5.26 (RR_{99}; CI 4.30 to 7.85). This implies that heavy or extreme frontal rainfall is expected to emerge more frequently owing to the greenhouse gas warming effects (*1*, *30*). The FAR_{95} and FAR_{99} were 0.66 (CI 0.61 to 0.66) and 0.81 (CI 0.77 to 0.87), respectively. Since FAR is defined as the extent to which the event is attributable to anthropogenic activity, the results showed that the EASM frontal heavy and extreme rainfall have been intensified primarily by anthropogenically induced global warming.

Next, we applied the fingerprint analysis to examine the signal of anthropogenic impact on the EASM front precipitation system and to assess its temporal evolution (see Materials and Methods). A signal (s) was detected from the annual mean of FRI based on the difference between the HIST and the XGHG simulations, which is defined as the anthropogenic impact fingerprint. The increase in s suggests that the anthropogenic warming signal is strengthening. We found that the increasing trend of s based on observed data (s_{OBS}) was notably greater than the signal detected in the XGHG experiment (s_{XGHG}; $P < 0.01$) (Fig. 2). This implies that the strengthened s_{OBS} is unlikely to emerge without the greenhouse gas emission (i.e., XGHG experiments). The observed s_{OBS} was explained by the fingerprint extracted from the HIST experiment (s_{HIST}), which points to the greenhouse forcing effect. These results suggest a robust anthropogenic influence on the enhancement of FRI over EA during the historical period.

Physical mechanisms of intensified frontal rainfall

The EA summer rainfall variability is predominately affected by the location, intensity, and shape of the WNPSH (*22*, *23*, *38*). Along the western rim of the WNPSH, southwesterly moisture transport from the South China Sea and the Philippine Sea to the East China Sea provides a crucial source of precipitable water to the EASM front (*18*, *21*). To examine the effect of greenhouse gas on this WNPSH mechanism, we examined the differences of the composited sea level pressure, 500-hPa geopotential height, and 850-hPa moisture convergence fields between the HIST and the XGHG experiments (see Materials and Methods). During the later period (1991–2015), the HIST experiment compared to the XGHG experiment exhibited

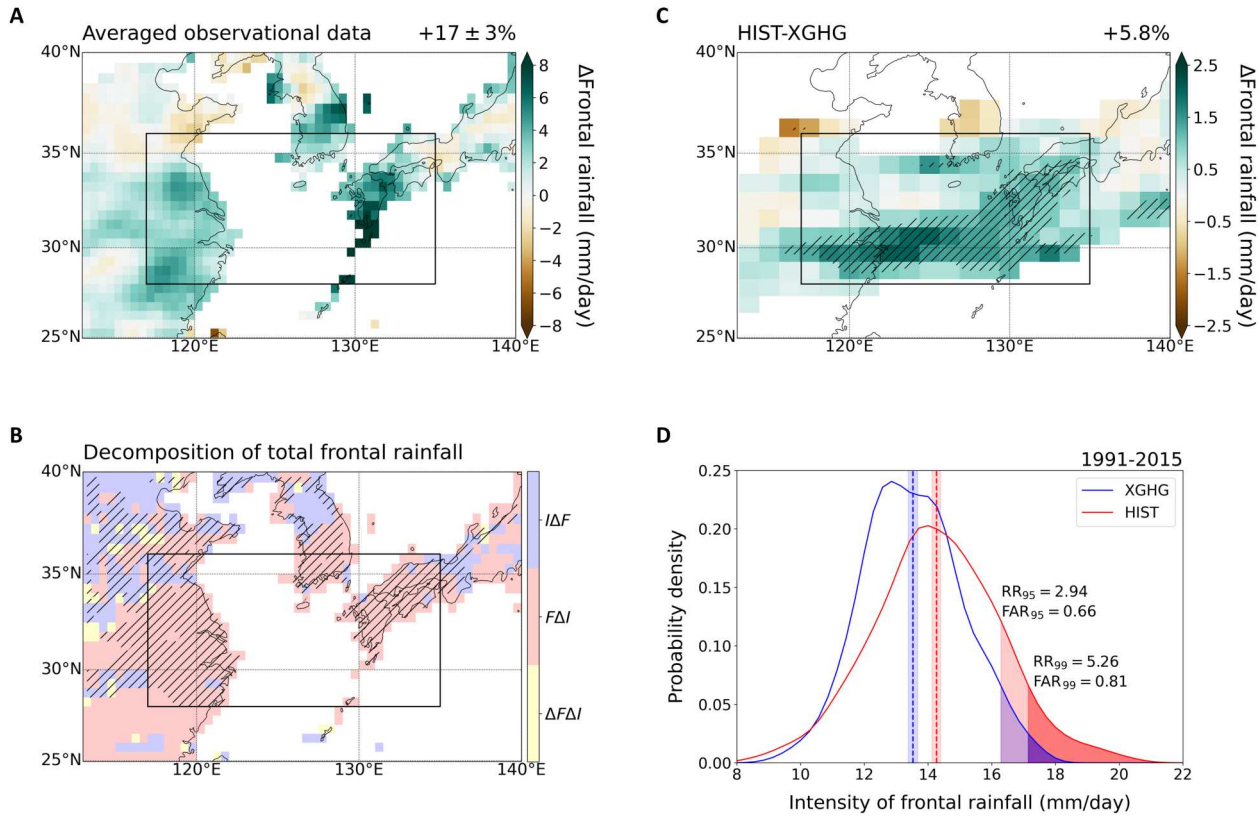

Fig. 1. Difference in the intensity of frontal rainfall (mm day^{-1}). (**A**) Observed difference in frontal rainfall intensity (FRI) from the later (1991–2015) to the earlier periods (1958–1982) derived from the averaged results of both APHRODITE and REGEN datasets. (**B**) Dominant term to changes in total frontal rainfall over each grid. The terms representing change in frequency ($I\Delta F$; blue), change in intensity ($F\Delta I$; red), and change in covariation ($\Delta F\Delta I$; yellow) account for more than 50% of changes in total frontal rainfall based on the APHRODITE dataset. Observed changes are computed between the early (1958–1982) and late (1991–2015) periods. The hatch represents the grid where a change in FRI ($F\Delta I$) is a dominant term (>50% contribution threshold) for the change in total frontal rainfall in the later period (1991–2015) based on model experiments (HIST-XGHG). (**C**) Difference of FRI between ensemble averages of historical (HIST) and nongreenhouse gases (XGHG) runs based on the CESM1-LE simulations during 1991–2015. Hatches in (B) and (C) indicate statistical significance at the 95% confidence level. The box represents the targeted domain (28°N-36°N, 117°E-135°E). Changing rates (%) of FRI in the targeted domain are shown in the upper right corner. The FRI is shown considering the frequency (>10%) of frontal rainfall. (**D**) Probability density distribution of the intensity of frontal rainfall over the targeted domain [boxes in (A) to (C)] including the ocean during 1991–2015. Blue and red lines are for XGHG and HIST runs, respectively. The vertical dashed line and shading represent the average and 95% confidence interval (CI) of the FRI from 1000 bootstrap resampling, respectively. Shaded area indicates the frontal rainfall corresponding to the 95th and 99th percentiles based on the XGHG simulations. The risk ratio (RR) and fraction of attributable risk (FAR) are shown based on the 95th and 99th percentiles based on XGHG simulations.

readily recognizable enhancements in WNPSH (+22.8 gpm) and moisture transport (+8.7 g/kg m/s) over EA (fig. S10B). In contrast, during the earlier period (1958–1982), these features were rather weak and marginal, with a difference in WNPSH of +7.9 gpm and moisture transport of +4.2 g/kg m/s (fig. S10A). This confirms the existence of even more favorable conditions for the frontal precipitation in the later period than before.

To reveal the effect of anthropogenic warming on frontal rainfall, the differences (HIST-XGHG) of sea level pressure and moisture flux were regressed onto the change of FRI within the targeted domain (box in Fig. 1A) during 1991–2015 (Fig. 3A). Anthropogenic greenhouse gas forcing likely intensified frontal rainfall by strengthening the WNPSH and enhancing moisture transport from the tropics to EA. Meanwhile, the upper-level cyclonic circulation anomalies together with the lower-level circulations contribute to the enhancement of southwesterly flows and associated moisture transport (*39*). In addition, such a response of regional climate patterns to the anthropogenic greenhouse gas forcing was analogous to the spatial patterns of the observed changes in the atmospheric conditions during the historical periods (fig. S11).

Further, we investigated the temporal variations of two major factors, lower-level moisture flux convergence (MFC; 22°N-33°N, 115°E-135°E) and the intensity of the WNPSH. The impact of global warming on the intensity of the WNPSH remains highly uncertain (*40*–*42*). Here, the WNPSH index was calculated on the basis of the difference in sea level pressure between two regions: the western North Pacific (15°N-25°N, 137°E-153°E) and East Asia (26°N-36°N, 117°E-133°E). This definition provides a way to assess the relative strength of the WNPSH at the synoptic scale. In the later period (1991–2015), the intensity of the MFC and the WNPSH tend to be greater in the HIST than in the XGHG experiments (Fig. 3B) (*43*, *44*). To indicate the fundamental difference between the two simulations during the earlier and later periods, the joint and marginal distributions of simulation ensembles from the HIST and the XGHG experiments were illustrated for the linear slope of the MFC and the WNPSH (Fig. 4). With the greenhouse gas

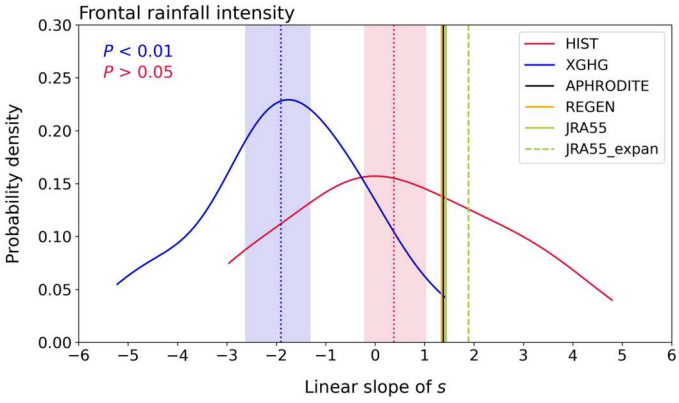

Fig. 2. Linear slope of detection signal *s*. Probability density distribution of linear slope of detection signals (*s*) based on the XGHG (blue) and HIST (red) runs for 1991–2015. Vertical dotted lines and shades are the averages and 95% CI obtained from 1000 bootstrap resampling, respectively. Vertical black, orange, and green lines show the linear slope of *s* based on APHRODITE, REGEN, and JRA55, respectively. Dashed green line indicates the linear slope of *s* for the longer period of 1991–2020 based on the JRA55. The upper left corner displays the probability (*P*) of exceeding the observed value for the XGHG (blue) and HIST (red) results. The detection signal *s* is defined from the nonoptimized fingerprint analysis of frontal rainfall intensity (FRI).

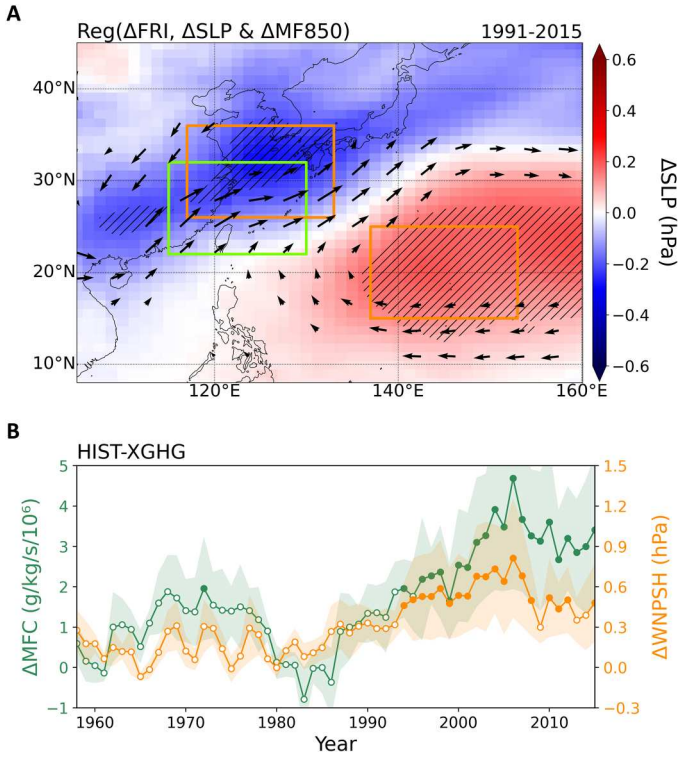

Fig. 3. Enhancement of frontal rainfall related to differences in sea level pressure and moisture flux between the HIST and the XGHG experiments. (**A**) Regression coefficient of differences (HIST-XGHG) in sea level pressure (SLP; shading, hPa) and moisture flux at 850 hPa (MF850; vector, g/kg m/s) against the difference (HIST-XGHG) of normalized frontal rainfall intensity (FRI) over the targeted domain (28°N-36°N, 117°E-135°E) during 1991–2015. All variables were detrended. Hatches and vectors indicate statistical significance at a 95% confidence level based on Student's *t* test. (**B**) Time series of differences (HIST-XGHG) of ensemble average for moisture flux convergence (MFC; green, g/kg/s/10^6) and WNPSH (orange, hPa) indices during 1958–2015. Seven-year moving window average is applied. Open and closed circles indicate statistical significance at a 95% confidence level based on Student's *t* test. MFC index is defined as area-averaged MFC at 850 hPa over the green box (22°N-32°N, 115°E-130°E), and the WNPSH index is given by the SLP averaged over the western North Pacific (15°N-25°N, 137°E-153°E) minus that averaged over East Asia (26°N-36°N, 117°E-133°E) as shown in orange boxes in (A). Shades show the spread between ensemble members.

forcing, the increasing rate of WNPSH was higher and more notable in the later period (0.03 Pa/year with interquartile range of −0.02 to 0.06 Pa/year) than in the earlier period (−0.01 Pa/year with interquartile range of −0.04 to 0.03 Pa/year). The increasing trend of moisture convergence was also captured in the HIST during the later period, although no substantial difference between the HIST and the XGHG experiments was observed in the earlier period. Thus, the difference between the two simulations was more apparent in the recent historical period (1991–2015).

Given that the underlying dynamics of the atmospheric circulations are driven by differential heating of the land-sea thermal contrast areas (*38*), it is likely that the strengthened meridional wind can modulate the EASM frontal rainfall (fig. S12C) in response to anthropogenic warming (*45*, *46*). This process can form the outcome of favorable conditions leading to the increase in frontal rainfall. To examine this, we conducted a moisture budget analysis for the lower atmosphere (i.e., 850-hPa) (*47*). By using the moisture budget analysis (see Materials and Methods), we investigated the respective contributions of the dynamic and thermodynamic factors to the atmospheric moisture content changes. As shown in fig. S12, anthropogenic warming led to the increase in frontal rainfall by controlling the thermodynamic component to the EASM precipitation (83.4%). The abundant water vapor induced by increasing temperature under the Clausius-Clapeyron relation contributes to the enhanced precipitation, as well, but the changes in moisture convergence are more pronouncedly modulated by greenhouse gas forcing (*48*). Although the dynamic component can suppress the increasing rainfall owing to atmospheric stabilization (*47*, *49*), it plays an important role in increasing the intensity of EASM frontal rainfall through moisture pooling and water vapor flux convergence. Therefore, with the help of the thermodynamic component, the dynamic component such as the WNPSH and moisture transport play a crucial role to intensify the EASM frontal precipitation system.

DISCUSSION

This study is the first to synoptically attribute the anthropogenic greenhouse gas impact on the EASM frontal precipitation system using objectively detected frontal rainfall. On the basis of both the observation and large ensemble model simulations with the fingerprint analysis, we showed that the EASM frontal rainfall was enhanced mainly in response to climate change associated with anthropogenic greenhouse gas emissions. Disentangling changes in frontal rainfall requires a more comprehensive analysis of various aspects. Our study revealed a marginal increase in both the occurrence of the detected front (+1.8%; fig. S5C) and the frequency of frontal rainfall (+1.1%; fig. S6A) in the later period (1991–2015) based on observation. Furthermore, there was an increase in the ratio of frontal rainfall relative to total rainfall (+1.3%; fig. S6B). These findings imply that the intensity of EA frontal rainfall has been further strengthened, since the contribution of other factors

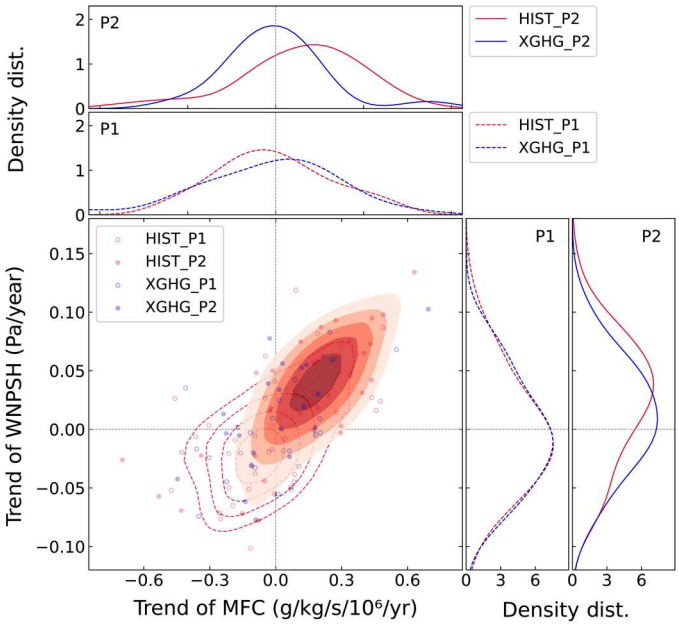

Fig. 4. Changes in MFC and WNPSH based on HIST and XGHG runs. Trend and probability density distribution of MFC (g/kg/s/10^6/year) and WNPSH (Pa/year) indices during the earlier [1958–1982 (P1)] and later [1991–2015 (P2)] periods based on HIST (red) and XGHG (blue) experiments. Open and closed circles represent the simulated values during P1 and P2, respectively. The dashed contour and shading indicate the joint probability distribution of MFC and anomalous WNPSH trends during P1 and P2 based on HIST experiment, respectively.

were marginal compared to the intensity increase. Thus, we have suggested that intensified moisture transport and the WNPSH contribute to enhancing FRI by providing sufficient moisture over EA under the warmer climate. As a further study, investigating the changes in the number of strong fronts is expected to provide insights into extreme frontal rainfall events (*50*).

While we have carefully validated the simulated data, a potential drawback still exists because we used large ensemble simulations derived from a single model. The results derived from CMIP5 and CMIP6 models project an increase in summer water vapor transport in EA under future global warming scenarios with medium confidence (*42*, *51*). However, the projection of WNPSH remains uncertain and displays intermodal spread. The WNPSH driven by sea level pressure projects to intensify in the warm climate due to the land-sea thermal contrast with low confidence (*42*, *52*). These mechanisms, which contribute to increased EA precipitation under future warming, align with the mechanism delineated in this study, as EA frontal rainfall increases during the investigated period of 1958–2015. Despite the constraints of model use, our findings point toward increased moisture transport and enhanced WNPSH.

Note that this study is dependent on the methodology used to detect fronts and attribute precipitation to fronts. The atmospheric fronts play a vital role in driving the seasonal and regional variation of weather on a daily scale, particularly in the midlatitude (*19*, *53*–*55*). Understanding the changes in synoptic weather systems and associated precipitation events is essential for our society to adapt to future climate changes (*15*, *56*, *57*). Furthermore, the system-oriented detection and attribution approach can be applicable to other types of weather systems such as tropical cyclones (*58*, *59*).

There are various aspects that could be studied further, as we have only focused on the anthropogenic greenhouse gas impacts. The negative value observed in the linear slope of s_{XGHG} implies the potential influence of factors beyond greenhouse gas forcing on the reduction of FRI (Fig. 2). In the field of detection and attribution of precipitation changes, several studies have shown that aerosol forcing has played a mitigating role by reducing precipitation (*60*, *61*). Thus, quantifying the relative importance of other climate forces (i.e., anthropogenic aerosol, land use, and land type) (*61*–*63*) that contribute to EA summer frontal rainfall can be the next study. At the Conference of the Parties (COP27) of the United Nations Framework Convention on Climate Change (UNFCCC) in Egypt, defining "loss and damage" to finance for recovery from climate disasters was on the key agenda for the first time. Our study could provide ways for implementing an assessment framework for a quantitative and system-based attribution of human-induced global warming at the regional scale.

MATERIALS AND METHODS

Observational datasets

To identify fronts, 6-hourly data obtained from the 55-year Japanese Reanalysis Project (JRA55) (*64*) with 1.25 × 1.25 horizontal resolutions were analyzed for the period of 1958–2020. This study separates two historical periods to account for the long-term changes: earlier (1958–1982) and later periods (1991–2015). For the observed precipitation data, we used the APHRODITE Monsoon Asia V1101 and extension V1101EX_R1 precipitation dataset (*34*) from 1958–2015. The APHRODITE applies daily grid precipitation data over the Asian land domain with a high spatial resolution (0.5° horizontal resolution) based on rain-gauge observations. It is considered a benchmark for validating the precipitation obtained from satellite and model simulations (*65*). Furthermore, we compared its precipitation data with an interpolated network of in situ data called REGEN dataset (*66*) to validate the APHRODITE dataset. Both datasets exhibited similar patterns with PCCs of 0.89 and 0.48 for the climatological mean and interannual variability (SD) of precipitation during the active EASM frontal season (16 June to 15 July) in 1958–2015, respectively (fig. S13). In addition, the REGEN dataset indicated an increase in FRI, which showed a comparable pattern (PCC of 0.72) to that observed in the APHRODITE dataset (Fig. 1A and fig. S4C).

CESM1 large ensemble dataset

We analyzed large ensemble simulations from the Community Earth System Model 1 (CESM-LE) (*32*) under the CMIP5 HIST (1958–2005), future Representative Concentration Pathway (RCP) 8.5 W m^{-2} radiative forcing scenario (2006–2015), and XGHG (1958–2015) forcing simulations with 0.9° × 1.25° horizontal grid resolution. To identify the role of greenhouse gas forcing on the intensity and frequency of frontal rainfall, we used the "all-but-one" experiments. We mainly investigated the HIST and XGHG (*31*) ensembles, which comprised 40 and 20 members, respectively. The XGHG has conducted the same forcing protocol as HIST, except that greenhouse gas forcing was fixed at the level in 1920 conditions. The influence of the greenhouse gases-only forcing on frontal rainfall can thus be inferred by the differences between HIST and

XGHG projections. The CESM-LE shows a well-reproduced spatial distribution of the annual mean precipitation and interannual variability (*60*, *67*). The changes in precipitation simulated CESM-LE generally align with the observed results, although there are some differences at regional scale (*60*, *68*). Despite the inherent biases in precipitation, the models capture the response to anthropogenic greenhouse gas forcing, in particular in relation to weather systems like frontal rainfall (*54*, *68*). Notably, the model exhibits a remarkable ability to reproduce reasonable patterns of FRI in terms of the climatological mean and standardized deviations between each member of the HIST experiment and two observed datasets (APHRODITE and REGEN) during 1958–2015 (fig. S14). The patterns of FRI derived from the ensemble mean of the HIST demonstrate a high degree of similarity (PCC of 0.68) to those observed. In addition, the internal variability of FRI within the targeted domain is 0.86 mm day^{-1}.

Detection of the front and frontal rainfall

The front was detected from the JRA55 data at a 6-hourly time step. We followed the front definition of Li *et al.* (*18*) with some modifications made for the comparison with Japan Meteorological Agency (JMA) weather maps (figs. S1 and S2). The general fronts are accompanied by a strong equivalent potential temperature gradient along the rain band. Thus, the meridional gradient of equivalent potential temperature is the primary variable to detect the frontline. The fronts were detected as follows.

(1) The absolute value of the meridional gradient of equivalent potential temperature at 850-hPa ($|\partial\theta_e/\partial y|$) was greater than 0.04 K km^{-1} for excluding a priori regions of weak thermal gradient (*18*, *53*, *69*).

(2) The number of grids satisfying condition (1) was greater than 10% of the total number of grids in the study domain to prevent the identification of nonsynoptic fronts (*50*, *53*, *69*).

(3) The averaged difference of the median latitude of individual longitude (LAT_i) was less than the horizontal resolution, where i refers to the west-to-east ith longitude in the study domain. In this study, a threshold of $\overline{|LAT_{i+1} - LAT_i|} < 1.25$ was applied, as the horizontal resolution of JRA55 is 1.25°.

(4) The front was detected as the running average of LAT_i.

To verify our front detection, we used the front information based on the surface weather chart (*17*), which was published by the forecasters in the JMA during 2001–2010 (fig. S1). The reanalysis data and CESM1-LE projections successfully simulated the location of the median latitude of the front over the EA region (Supplementary Text and fig. S2). This study focused on the active EASM front season, from the second half of June (June 16) to the first half of July (July 15) along 30°N latitude.

The frontal precipitation, which corresponds to about 40% of the EASM, is defined as the daily precipitation within a 500-km radius from the front line at any timestep of the day (*19*, *57*). Here, we only considered the wet frontal rainfall (intensity of frontal precipitation >1 mm day^{-1}). To further understand the possible mechanisms of projected increasing frontal rainfall, we compared several variables (e.g., moisture transport, geopotential height, and MFC) when the intensity of daily frontal rainfall over the EASM front region (28°N-36°N, 117°E-135°E) was >1 mm day^{-1} using HIST and XGHG experiments (Figs. 3 and 4).

Decomposition of changes in total frontal mean rainfall

The total precipitation (PR) was composed of mean intensity (I; mm day^{-1}) and frequency (F; total number of occurrences) of precipitation (PR = $F \cdot I$). To identify the main contributor to changes in frontal rainfall, differences in the accumulated PR can be expressed as (*15*):

$$\begin{aligned}\Delta PR &= PR' - PR = (F + \Delta F) \cdot (I + \Delta I) - F \cdot I \\ &= \Delta F \cdot I + F \cdot \Delta I + \Delta F \cdot \Delta I\end{aligned}$$

where Δ indicates the difference in the frontal rainfall between HIST and XGHG runs. The prime indicates the HIST run. The change in PR between the two simulations is decomposed into frequency ($\Delta F \cdot I$), intensity ($F \cdot \Delta I$), and covariation terms ($\Delta F \cdot \Delta I$). In the case of the reanalysis dataset, the changes in PR were investigated between the historical earlier (1958–1982) and later (1991–2015) periods. Through the decomposition of total frontal rainfall, we determined that enhancement of FRI is the key component to increase the EASM frontal rainfall in the historical later period (fig. S3) and in HIST simulations (fig. S7).

RR and FAR

The RR and FAR are defined as the ratio of the probability of occurrence of extreme events in historical (P_{HIST}) and nongreenhouse gas forcing effect (P_{XGHG}) to assess the greenhouse gas impact on extreme events. RR is defined as RR = P_{HIST}/P_{XGHG}, where P_{HIST} and P_{XGHG} are the probability of exceeding a certain quantile (for example, 95th and 99th percentile) based on XGHG simulations during the later (1991–2015) period.

FAR is defined as FAR = $1 - (P_{XGHG}/P_{HIST})$. RR is simply a ratio of the occurrence of extreme events but FAR shows how much of the extreme event can be attributed to external influence (*37*). The positive (negative) FAR indicates that anthropogenic greenhouse gas has intensified (suppressed) the occurrence of frontal heavy rainfall. When FAR is close to one, it implies that anthropogenic greenhouse gas is likely to intensify the frontal heavy rainfall event. Here, we calculated the probability of exceeding the 95th and 99th percentile at area averaged over the targeted domain (28°N-36°N, 117°E-135°E) based on P_{XGHG} during the active EASM front season in the later period. The 95th and 99th percentile thresholds of FRI were found to be 16.0 and 17.1 mm/day, respectively. The uncertainty in likelihood ratio method was estimated for the 5 to 95% CIs of RR and FAR based on the 1000 bootstrap resampling (*1*).

Fingerprint analysis

The nonoptimized version of the fingerprint analysis technique was used to identify the climate change signal (*56*). This technique can detect the climate change signal contained in the observed or modeled spatial patterns. The detection signal (s) can be estimated as

$$s(t) = \mathrm{FRI}(x, y, t) \cdot f(x, y)$$

where FRI indicates the frontal rainfall intensity and f is a fingerprint, respectively. x is longitude and y is latitude over 1.25° × 1.25° horizontal resolution. t denotes time with a unit year and the targeted study domain is the EA region (25°N-40°N, 110°E-140°E). The dot denotes the dot-product operation. The fingerprint, which shows the spatial pattern of climate change impacts, was

estimated as follows:

$$f(x,y) = f'(x,y)/|f'(x,y)|$$

where f' is the composite difference in the FRI between the HIST and XGHG runs for 1991–2015. Considering the significance, f was set to 0 for statistically insignificant grid points at the 90% confidence level. The f was analyzed over land grid points because fingerprint analysis was performed on the basis of the in situ observation (fig. S15). Furthermore, s and FRI were calculated using XGHG, HIST, and the observed dataset during 1958–2015. As an increase in s indicates the strength of the anthropogenic climate change impact signal, the linear slope of s during 1958–2015 can distinguish the climate change impacts on FRI. When the observation slope was larger than that of nongreenhouse gas forcing (XGHG) simulations, the anthropogenic climate change signal was distinguished. Because the APHRODITE precipitation data were covered until 2015, the expanded (1991–2020) precipitation from JRA55 was also investigated (green line in Fig. 2). We set the null hypothesis that the observed detection signal was due to the nongreenhouse forcing effects and applied a one-tailed test with a 5% significance level.

Horizontal MFC

To identify the roles of thermodynamic (due to moisture change) and dynamic (due to atmospheric circulation) effects in frontal precipitation changes over EA, we decomposed the horizontal MFC (HMFC) at 850 hPa (*47*)

$$\delta\mathrm{HMFC}_{850} = \delta\mathrm{TH}_{850} + \delta\mathrm{DY}_{850} + \delta\mathrm{TE}_{850} + \mathrm{Res.}$$

$$\delta\mathrm{TH}_{850} = -\nabla\cdot(\overline{u_{\mathrm{XGHG}}}\ [\delta\overline{q}])_{850}$$

$$\delta\mathrm{DY}_{850} = -\nabla\cdot([\delta\overline{u}]\ \overline{q_{\mathrm{XGHG}}})_{850}$$

$$\delta\mathrm{TE}_{850} = -\nabla\cdot\delta(\overline{u'q'})_{850}$$

$$\delta(\cdot) = (\cdot)_{\mathrm{HIST}} - (\cdot)_{\mathrm{XGHG}}$$

where u is the horizontal vector wind and q is the specific humidity. The HMFC can be divided into thermodynamic (δTH), dynamic (δDY), transient eddy (δTE), and residual (Res.) terms. The overbar indicates the climatological mean, and the prime indicates the departure from the climatological mean during 1991–2015. Note that we only focus on the frontal rainfall over the targeted domain (28°N-36°N, 117°E-135°E) during the active EASM front season (June 16 to July 15). The subscripts 850, HIST, and XGHG indicate the variables at 850 hPa, the ensemble mean from CESM1-LE HIST, and XGHG runs, respectively. Although this approach omits the vertical integration of the whole atmospheric column owing to the CESM1-LE data limitation, the HMFC at 850-hPa can represent reasonable patterns similar to the vertically integrated MFC over EA (fig. S12) (*70*).

Supplementary Materials

This PDF file includes:

Supplementary Text
Figs. S1 to S15

REFERENCES AND NOTES

1. S.-K. Min, S.-Y. Jo, M.-G. Seong, Y.-H. Kim, S.-W. Son, Y.-H. Byun, F. C. Lott, P. A. Stott, Human contribution to the 2020 summer successive hot-wet extremes in South Korea. *Bull. Am. Meteorol. Soc.* **103**, S90–S97 (2022).
2. W. Zeng, G. Chen, L. Bai, Q. Liu, Z. Wen, Multiscale processes of heavy rainfall over East Asia in summer 2020: Diurnal cycle in response to synoptic disturbances. *Mon. Weather Rev.* **150**, 1355–1376 (2022).
3. S. S. Y. Wang, H. Kim, D. Coumou, J. H. Yoon, L. Zhao, R. R. Gillies, Consecutive extreme flooding and heat wave in Japan: Are they becoming a norm? *Atmos. Sci. Lett.* **20**, e933 (2019).
4. H. G. Takahashi, H. Fujinami, Recent decadal enhancement of Meiyu–Baiu heavy rainfall over East Asia. *Sci. Rep.* **11**, 13665 (2021).
5. H. Tsuguti, N. Seino, H. Kawase, Y. Imada, T. Nakaegawa, I. Takayabu, Meteorological overview and mesoscale characteristics of the Heavy Rain Event of July 2018 in Japan. *Landslides* **16**, 363–371 (2019).
6. A. Shimpo, K. Takemura, S. Wakamatsu, H. Togawa, Y. Mochizuki, M. Takekawa, S. Tanaka, K. Yamashita, S. Maeda, R. Kurora, H. Murai, N. Kitabatake, H. Tsuguti, H. Mukougawa, T. Iwasaki, R. Kawamura, M. Kimoto, I. Takayabu, Y. N. Takayabu, Y. Tanimoto, T. Hirooka, Y. Masumoto, M. Watanabe, K. Tsuboki, H. Nakamura, Primary factors behind the Heavy Rain Event of July 2018 and the subsequent heat wave in Japan. *SOLA* **15A**, 13–18 (2019).
7. K. Wei, C. Ouyang, H. Duan, Y. Li, M. Chen, J. Ma, H. An, S. Zhou, Reflections on the catastrophic 2020 Yangtze River Basin flooding in Southern China. *Innovation* **1**, 100038 (2020).
8. Y. Takaya, I. Ishikawa, C. Kobayashi, H. Endo, T. Ose, Enhanced Meiyu-Baiu rainfall in early summer 2020: Aftermath of the 2019 super IOD event. *Geophys. Res. Lett.* **47**, e2020GL090671 (2020).
9. Y. Ma, Z. Hu, X. Meng, F. Liu, W. Dong, Was the record-breaking Mei-yu of 2020 enhanced by regional climate change? *Bull. Am. Meteorol. Soc.* **103**, S76–S82 (2022).
10. C. Park, S.-W. Son, H. Kim, Y.-G. Ham, J. Kim, D.-H. Cha, E.-C. Chang, G. Lee, J.-S. Kug, W.-S. Lee, Y.-Y. Lee, H. C. Lee, B. Lim, Record-breaking summer rainfall in South Korea in 2020: Synoptic characteristics and the role of large-scale circulations. *Mon. Weather Rev.* **149**, 3085–3100 (2021).
11. Gawon Bae, Jessie Yeung, Record rainfall kills at least 9 in Seoul as water floods buildings, submerges cars. CNN (2022); https://www.cnn.com/2022/08/09/asia/seoul-south-korea-rain-flooding-intl-hnk).
12. T. Zhou, L. Ren, W. Zhang, Anthropogenic influence on extreme Meiyu rainfall in 2020 and its future risk. *Sci. China Earth Sci.* **64**, 1633–1644 (2021).
13. Q. Yuan, G. Wang, C. Zhu, D. Lou, D. F. T. Hagan, X. Ma, M. Zhan, Coupling of soil moisture and air temperature from multiyear data during 1980-2013 over China. *Atmos.* **11**, 25 (2020).
14. D.-Y. Gong, C.-H. Ho, Arctic oscillation signals in the East Asian summer monsoon. *J. Geophys. Res.* **108**, 10.1029/2002JD002193, (2003).
15. N. Utsumi, H. Kim, S. Kanae, T. Oki, Which weather systems are projected to cause future changes in mean and extreme precipitation in CMIP5 simulations? *J. Geophys. Res.* **121**, 10522–10537 (2016).
16. T. C. Chen, S. Y. Wang, W. R. Huang, M. C. Yen, Variation of the East Asian summer monsoon rainfall. *J. Climate* **17**, 744–762 (2004).
17. N. Utsumi, H. Kim, S. Seto, S. Kanae, T. Oki, Climatological characteristics of fronts in the western North Pacific based on surface weather charts. *J. Geophys. Res. Atmos.* **119**, 9400–9418 (2014).
18. Y. Li, Y. Deng, S. Yang, H. Zhang, Multi-scale temporospatial variability of the East Asian Meiyu-Baiu fronts: Characterization with a suite of new objective indices. *Climate Dynam.* **51**, 1659–1670 (2018).
19. J. L. Catto, C. Jakob, G. Berry, N. Nicholls, Relating global precipitation to atmospheric fronts. *Geophys. Res. Lett.* **39**, L10805 (2012).
20. K.-J. Ha, S. K. Park, K. Y. Kim, On interannual characteristics of climate prediction center merged analysis precipitation over the Korean Peninsula during the summer monsoon season. *Int. J. Climatol.* **25**, 99–116 (2005).
21. B. Wang, L. Ho, Rainy season of the Asian–Pacific summer monsoon. *J. Climate* **15**, 386–398 (2002).
22. C.-P. Chang, Y. Zhang, T. Li, Interannual and interdecadal variations of the East Asian summer monsoon and tropical pacific SSTs. Part I: Roles of the subtropical ridge. *J. Climate* **13**, 4310–4325 (2000).
23. D. Yihui, J. C. L. Chan, The East Asian summer monsoon: An overview. *Meteorol. Atmos. Phys.* **89**, 117–142 (2005).
24. S. Dong, Y. Sun, X. Zhang, S.-K. Min, Y.-H. Kim, Attribution of extreme precipitation with updated observations and CMIP6 simulations. *J. Climate* **34**, 871–881 (2021).

25. K.-J. Ha, B.-H. Kim, E.-S. Chung, J. C. L. Chan, C.-P. Chang, Major factors of global and regional monsoon rainfall changes: Natural versus anthropogenic forcing. *Environ. Res. Lett.* **15**, 034055 (2020).
26. J. Park, H. Kim, S.-Y. Simon Wang, J.-H. Jeong, K.-S. Lim, M. Laplante, J.-H. Yoon, Intensification of the East Asian summer monsoon lifecycle based on observation and CMIP6. *Environ. Res. Lett.* **15**, 0940b9 (2020).
27. Y. Satoh, K. Yoshimura, Y. Pokhrel, H. Kim, H. Shiogama, T. Yokohata, N. Hanasaki, Y. Wada, P. Burek, E. Byers, H. M. Schmied, D. Gerten, S. Ostberg, S. N. Gosling, J. E. S. Boulange, T. Oki, The timing of unprecedented hydrological drought under climate change. *Nat. Commun.* **13**, 3287 (2022).
28. H. Kawase, Y. Imada, H. Sasaki, T. Nakaegawa, A. Murata, M. Nosaka, I. Takayabu, Contribution of historical global warming to local-scale heavy precipitation in western Japan estimated by large ensemble high-resolution simulations. *J. Geophys. Res. Atmos.* **124**, 6093–6103 (2019).
29. Y. Kamae, Y. Imada, H. Kawase, W. Mei, Atmospheric rivers bring more frequent and intense extreme rainfall events over East Asia under global warming. *Geophys. Res. Lett.* **48**, e2021GL096030 (2021).
30. S. K. Min, X. Zhang, F. W. Zwiers, G. C. Hegerl, Human contribution to more-intense precipitation extremes. *Nature* **470**, 378–381 (2011).
31. C. Deser, A. S. Phillips, I. R. Simpson, N. Rosenbloom, D. Coleman, F. Lehner, A. G. Pendergrass, P. Dinezio, S. Stevenson, Isolating the evolving contributions of anthropogenic aerosols and greenhouse gases: A new CESM1 large ensemble community resource. *J. Climate* **33**, 7835–7858 (2020).
32. J. E. Kay, C. Deser, A. Phillips, A. Mai, C. Hannay, G. Strand, J. M. Arblaster, S. C. Bates, G. Danabasoglu, J. Edwards, M. Holland, P. Kushner, J. F. Lamarque, D. Lawrence, K. Lindsay, A. Middleton, E. Munoz, R. Neale, K. Oleson, L. Polvani, M. Vertenstein, The Community Earth System Model (CESM) large ensemble project: A community resource for studying climate change in the presence of internal climate variability. *Bull. Am. Meteorol. Soc.* **96**, 1333–1349 (2015).
33. S.-Y. Wang, A. J. Clark, NAM model forecasts of warm-season quasi-stationary frontal environments in the central United States. *Weather Forecast.* **25**, 1281–1292 (2010).
34. A. Yatagai, K. Kamiguchi, O. Arakawa, A. Hamada, N. Yasutomi, A. Kitoh, Aphrodite constructing a long-term daily gridded precipitation dataset for Asia based on a dense network of rain gauges. *Bull. Am. Meteorol. Soc.* **93**, 1401–1415 (2012).
35. J. L. Catto, C. Jakob, N. Nicholls, Can the CMIP5 models represent winter frontal precipitation? *Geophys. Res. Lett.* **42**, 8596–8604 (2015).
36. E. Hawkins, R. Sutton, Time of emergence of climate signals. *Geophys. Res. Lett.* **39**, 10.1029/2011gl050087, (2012).
37. E. M. Fischer, R. Knutti, Anthropogenic contribution to global occurrence of heavy-precipitation and high-temperature extremes. *Nat. Clim. Chang.* **5**, 560–564 (2015).
38. H. Oh, K.-J. Ha, A. Timmermann, Disentangling impacts of dynamic and thermodynamic components on late summer rainfall anomalies in East Asia. *J. Geophys. Res. Atmos.* **123**, 8623–8633 (2018).
39. S. Y. S. Wang, Y. H. Lin, C. H. Wu, Interdecadal change of the active-phase summer monsoon in East Asia (Meiyu) since 1979. *Atmos. Sci. Lett.* **17**, 128–134 (2016).
40. C. He, T. Zhou, A. Lin, B. Wu, D. Gu, C. Li, B. Zheng, Enhanced or weakened Western North Pacific Subtropical High under global warming? *Sci. Rep.* **5**, 16771 (2015).
41. X. Chen, T. Zhou, P. Wu, Z. Guo, M. Wang, Emergent constraints on future projections of the western North Pacific Subtropical High. *Nat. Commun.* **11**, 2802 (2020).
42. Q. You, Z. Jiang, X. Yue, W. Guo, Y. Liu, J. Cao, W. Li, F. Wu, Z. Cai, H. Zhu, T. Li, Z. Liu, J. He, D. Chen, N. Pepin, P. Zhai, Recent frontiers of climate changes in East Asia at global warming of 1.5°C and 2°C. *NPJ Clim. Atmos. Sci.* **5**, 80 (2022).
43. J. Berner, H. M. Christensen, P. D. Sardeshmukh, Does ENSO regularity increase in a warming climate? *J. Climate* **33**, 1247–1259 (2020).
44. C. F. McSweeney, R. G. Jones, How representative is the spread of climate projections from the 5 CMIP5 GCMs used in ISI-MIP? *Clim. Serv.* **1**, 24–29 (2016).
45. K.-J. Ha, S. Moon, A. Timmermann, D. Kim, Future changes of summer monsoon characteristics and evaporative demand over Asia in CMIP6 simulations. *Geophys. Res. Lett.* **47**, e2020GL087492 (2020).
46. K. E. Trenberth, A. Dai, R. M. Rasmussen, D. B. Parsons, The changing character of precipitation. *Bull. Am. Meteorol. Soc.* **84**, 1205–1218 (2003).
47. S. Moon, K.-J. Ha, Future changes in monsoon duration and precipitation using CMIP6. *NPJ Clim. Atmos. Sci.* **3**, 45 (2020).
48. X. Li, M. Ting, C. Li, N. Henderson, Mechanisms of Asian summer monsoon changes in response to anthropogenic forcing in CMIP5 models. *J. Climate* **28**, 4107–4125 (2015).
49. H. Endo, A. Kitoh, Thermodynamic and dynamic effects on regional monsoon rainfall changes in a warmer climate. *Geophys. Res. Lett.* **41**, 1704–1711 (2014).
50. S. Schemm, M. Sprenger, O. Martius, H. Wernli, M. Zimmer, Increase in the number of extremely strong fronts over Europe? A study based on ERA-Interim reanalysis (1979–2014). *Geophys. Res. Lett.* **44**, 553–561 (2017).
51. Z. Xu, K. Fan, Projected changes in summer water vapor transport over East Asia under the 1.5°C and 2.0°C global warming targets. *AOSL* **12**, 124–130 (2019).
52. D. Huang, A. Liu, Y. Zheng, J. Zhu, Inter-model spread of the simulated East Asian summer monsoon rainfall and the associated atmospheric circulations from the CMIP6 models. *J. Geophys. Res. Atmos.* **127**, e2022JD037371 (2022).
53. R. Hénin, A. M. Ramos, S. Schemm, C. M. Gouveia, M. L. R. Liberato, Assigning precipitation to mid-latitudes fronts on sub-daily scales in the North Atlantic and European sector: Climatology and trends. *Int. J. Climatol.* **39**, 317–330 (2019).
54. K. Dagon, J. Truesdale, J. C. Biard, K. E. Kunkel, G. A. Meehl, M. J. Molina, Machine learning-based detection of weather fronts and associated extreme precipitation in historical and future climates. *J. Geophys. Res. Atmos.* **127**, e2022JD037038 (2022).
55. S. Niebler, A. Miltenberger, B. Schmidt, P. Spichtinger, Automated detection and classification of synoptic-scale fronts from atmospheric data grids. *Weather Clim.* **3**, 113–137 (2022).
56. N. Utsumi, H. Kim, Observed influence of anthropogenic climate change on tropical cyclone heavy rainfall. *Nat. Clim. Chang.* **12**, 436–440 (2022).
57. S. Rüdisühli, M. Sprenger, D. Leutwyler, C. Schär, H. Wernli, Attribution of precipitation to cyclones and fronts over Europe in a kilometer-scale regional climate simulation. *Weather Clim.* **1**, 675–699 (2020).
58. C. Kumler-Bonfanti, J. Stewart, D. Hall, M. Govett, Tropical and extratropical cyclone detection using deep learning. *J. Appl. Meteorol. Climatol.* **59**, 1971–1985 (2020).
59. A. M. Haberlie, W. S. Ashley, A method for identifying midlatitude mesoscale convective systems in radar mosaics. Part II: Tracking. *J. Appl. Meteorol. Climatol.* **57**, 1599–1621 (2018).
60. A. Zhao, D. S. Stevenson, M. A. Bollasina, Climate forcing and response to greenhouse gases, aerosols, and ozone in CESM1. *J. Geophys. Res. Atmos.* **124**, 13876–13894 (2019).
61. F. Tian, B. Dong, J. Robson, R. Sutton, Forced decadal changes in the East Asian summer monsoon: The roles of greenhouse gases and anthropogenic aerosols. *Climate Dynam.* **51**, 3699–3715 (2018).
62. R. Herbert, L. J. Wilcox, M. Joshi, E. Highwood, D. Frame, Nonlinear response of Asian summer monsoon precipitation to emission reductions in South and East Asia. *Environ. Res. Lett.* **17**, 014005 (2022).
63. M. Salzmann, Global warming without global mean precipitation increase? *Sci. Adv.* **2**, e1501572 (2016).
64. A. Ebita, S. Kobayashi, Y. Ota, M. Moriya, R. Kumabe, K. Onogi, Y. Harada, S. Yasui, K. Miyaoka, K. Takahashi, H. Kamahori, C. Kobayashi, H. Endo, M. Soma, Y. Oikawa, T. Ishimizu, The Japanese 55-year reanalysis "JRA-55": An interim report. *Sola* **7**, 149–152 (2011).
65. Z. Ma, J. Xu, Y. Ma, S. Zhu, K. He, S. Zhang, W. Ma, X. Xu, A long-term asian precipitation dataset (0.1°, 1-hourly, 1951–2015, Asia) anchoring the ERA5-land under the total volume control by APHRODITE. *Bull. Am. Meteorol. Soc.* **103**, E1146–E1171 (2022).
66. S. Contractor, M. G. Donat, L. V. Alexander, M. Ziese, A. Meyer-Christoffer, U. Schneider, E. Rustemeier, A. Becker, I. Durre, R. S. Vose, Rainfall Estimates on a Gridded Network (REGEN)–A global land-based gridded dataset of daily precipitation from 1950 to 2016. *Hydrol. Earth Syst. Sci.* **24**, 919–943 (2020).
67. J. L. Martel, A. Mailhot, F. Brissette, D. Caya, Role of natural climate variability in the detection of anthropogenic climate change signal for mean and extreme precipitation at local and regional scales. *J. Climate* **31**, 4241–4263 (2018).
68. F. Song, T. Zhou, Interannual variability of East Asian summer monsoon simulated by CMIP3 and CMIP5 AGCMs: Skill dependence on Indian Ocean-western pacific anticyclone teleconnection. *J. Climate* **27**, 1679–1697 (2014).
69. S. Schemm, I. Rudeva, I. Simmonds, Extratropical fronts in the lower troposphere-global perspectives obtained from two automated methods. *Q. J. Roy. Meteorol. Soc.* **141**, 1686–1698 (2015).
70. D. Lee, S.-K. Min, J. Jin, J.-W. Lee, D.-H. Cha, M.-S. Suh, J.-B. Ahn, S.-Y. Hong, H.-S. Kang, M. Joh, Thermodynamic and dynamic contributions to future changes in summer precipitation over Northeast Asia and Korea: A multi-RCM study. *Climate Dynam.* **49**, 4121–4139 (2017).

Acknowledgments

Funding: This work was supported by the National Research Foundation of Korea (NRF) grant funded by the Korea Government (MSIT) (2021H1D3A2A03097768). S.M. was supported by the NRF MSIT (2018R1A5A7025409). N.U. was supported by the Ministry of Education, Culture, Sports, Science and Technology of Japan (MEXT) KAKENHI (JP21H05178 and JP21H05002) and Japan Science and Technology Agency (JST) through the Belmont Forum (grant number JPMJBF2101). H.S. was supported by the Advanced Studies of Climate Change Projection (SENTAN, JPMXD0722680395) of MEXT. J.-H.J. and J.-H.Y. were supported by the Korea Meteorological Administration Research and Development Program under grant no. KMI2018-

07010. **Author contributions:** S.M. and H.K. designed the study and performed the analysis. All authors contributed to the writing of the manuscript. **Competing interests:** The authors declare that they have no competing interests. **Data and materials availability:** All data needed to evaluate the conclusions in this paper are present in the paper and/or the Supplementary Materials. The CESM1 Large Ensemble Projects simulation can be downloaded from https://cesm.ucar.edu/projects/community-projects/LENS/. The JRA55 reanalysis data can be downloaded from https://rda.ucar.edu/datasets/ds628.0/. APHRODITE precipitation data are accessible at http://aphrodite.st.hirosaki-u.ac.jp. REGEN precipitation data are available at https://dx.doi.org/10.25914/5ca4c380b0d44. All the detected front data are available at https://doi.org/10.22711/idr/971. The code for the EA front detection and figure production in this study is available at https://doi.org/10.5281/zenodo.8072940 and GitHub repository (https://github.com/suyeonmn/EASM_front.git). The data in this study are analyzed with NCAR Command Language (NCL; http://www.ncl.ucar.edu/).

Submitted 3 March 2023
Accepted 24 October 2023
Published 24 November 2023
10.1126/sciadv.adh4195

ScienceAdvances

Anthropogenic warming induced intensification of summer monsoon frontal precipitation over East Asia

Suyeon Moon, Nobuyuki Utsumi, Jee-Hoon Jeong, Jin-Ho Yoon, S.-Y. Simon Wang, Hideo Shiogama, and Hyungjun Kim

Sci. Adv. **9** (47), eadh4195. DOI: 10.1126/sciadv.adh4195

Science Advances (ISSN 2375-2548) is published by the American Association for the Advancement of Science. 1200 New York Avenue NW, Washington, DC 20005. The title *Science Advances* is a registered trademark of AAAS.